doi:10.26443/seismica.v3i2.1146

SEISMICA

Performance of synthetic DAS as a function of array geometry

Thomas W. Luckie * [1], **Robert W. Porritt** † [1]

[1]Sandia National Laboratories, Albuquerque, New Mexico, USA

Author contributions: *Conceptualization*: R. W. Porritt. *Data Curation*: T. W. Luckie. *Formal Analysis*: T. W. Luckie. *Funding Acquisition*: R. W. Porritt. *Investigation*: T. W. Luckie, R. W. Porritt. *Methodology*: T. W. Luckie, R. W. Porritt. *Project Administration*: R. W. Porritt. *Resources*: R. W. Porritt. *Software*: T. W. Luckie, R. W. Porritt. *Supervision*: R. W. Porritt. *Validation*: T. W. Luckie, R. W. Porritt. *Visualization*: T. W. Luckie, R. W. Porritt. *Writing – original draft*: T. W. Luckie. *Writing – review editing*: T. W. Luckie, R. W. Porritt.

Abstract Distributed Acoustic Sensing (DAS) can record acoustic wavefields at high sampling rates and with dense spatial resolution difficult to achieve with seismometers. Using optical scattering induced by cable deformation, DAS can record strain fields with spatial resolution of a few meters. However, many experiments utilizing DAS have relied on unused, dark telecommunication fibers. As a result, the geophysical community has not fully explored DAS survey parameters to characterize the ideal array design. This limits our understanding of guiding principles in array design to deploy DAS effectively and efficiently in the field. A better quantitative understanding of DAS array behavior can improve the quality of the data recorded by guiding the DAS array design. Here we use steered response functions, which account for DAS fiber's directional sensitivity, as well as beamforming and back-projection results from forward modelling calculations to assess the performance of varying DAS array geometries to record regional and local sources. A regular heptagon DAS array demonstrated improved capabilities for recording regional sources over other polygonal arrays, with potential improvements in recording and locating local sources. These results help reveal DAS array performance as a function of geometry and can guide future DAS deployments.

Production Editor: Gareth Funning
Handling Editor: Bradley Lipovsky
Copy & Layout Editor: Tara Nye

Received: November 2, 2023
Accepted: September 27, 2024
Published: October 31, 2024

Non-technical summary Distributed Acoustic Sensing (DAS) can record vibrations travelling through the Earth at high resolutions by repurposing fiber optic cables usually used for telecommunication. These recordings have higher sampling in space than what can be recorded using a traditional array of seismometers. However, many experiments using DAS have used pre-installed fiber optic cables, which prevents any kind of optimization in array design. This means that the scientific community has not had the opportunity to explore what shapes work best for detecting earthquakes with DAS. In this report, we test how well theoretical DAS shapes record simulated earthquakes. Our results show that a regular heptagon shape works best for detecting and locating earthquakes both near and far from this theoretical DAS cable. These results help reveal how DAS performs when the cable is buried in different shapes and which can guide scientists in designing a future DAS experiment.

1 Introduction

Distributed Acoustic Sensing (DAS) is a decade old technology that can record wavefields at high spatiotemporal resolution in a similar manner as traditional long-period, large-N seismic arrays. By measuring the strain field acting on a fiber optic cable, DAS can resolve signals with spatial resolution of a few meters (Lindsey and Martin, 2021). Compared to typically tens of meters to tens of kilometers spatial sampling of geophones and broadband seismometers, respectively, DAS provides a means to record wavefields at resolutions difficult, if not impossible, to achieve with traditional seismic instruments. As the seismic community begins to adapt to large-N deployments with the growing availability of high-quality nodal instruments, DAS presents itself as an endmember on this spectrum of instrument density.

Seismic DAS experiments work by repurposing fiber optic cables as multichannel arrays. An interrogator unit, installed at one end of an optical fiber, sends laser pulses into the fiber where impurities within the fiber result in Rayleigh backscattered light. The interrogator measures the phase shifts from this backscattered light in the time-domain in bins separated by what is called a gauge length, defined by the user during post-processing or set by the manufacturer during interrogator production, where light is collected over a certain amount of time. Thus, the interrogator collects data at virtual channels which are analogous to individual seismic stations. While DAS data is also reported at channels with sub-meter spacing, the conservatively estimated spatial resolution is fixed by the gauge length (Dou et al., 2017). As a result, the DAS array samples the strain field acting on the fiber coupled to the Earth at the meter scale over tens of kilometers of fiber.

DAS has been successfully used in a variety of geo-

*Corresponding author: twlucki@sandia.gov
†Corresponding author: rwporri@sandia.gov

physical applications, with cumulative data collected by DAS experiments over ~5 years outpacing ~30 years' worth of archived seismic data at the IRIS DMC (Lindsey and Martin, 2021; IRIS Data Management Center, 2023). Many of these previous DAS experiments have employed unused telecommunication fibers, resulting in little to no control over the array design (e.g., Lindsey et al., 2019; Fang et al., 2020; Wang et al., 2020; Baker and Abbott, 2022). As a result, the geophysical community has not fully explored DAS survey parameters to characterize the ideal DAS array design given specific experimental goals.

Recent work employing a custom designed and installed DAS array have demonstrated DAS's ability in regional (e.g., Wang et al., 2018) and global (e.g., Dando et al., 2022) seismic studies. The planned Rock Valley Direct Comparison (RV/DC) experiment (Snelson et al., 2022), a phase of the Source Physics Experiment (SPE; Snelson et al., 2013), aims to directly compare a shallow earthquake to a chemical explosion detonated at the same hypocenter, with DAS among the geophysical instrumentation to be used for observation. A better quantitative understanding of DAS array behavior prior to acquisition can improve the quality of the data recorded by guiding the DAS array design.

As the use of DAS grows in the geophysical community, understanding these array parameters is crucial if DAS is to be used on the same level as traditional seismic deployments. One of the most fundamental aspects to array design is the field layout. This encapsulates the geometry of the array, defined by parameters such as array size, length, direction, and instrument spacing. These parameters are tuned based on the specific questions motivating the experiment and logistical or field-based constraints, such as required resolution, noise conditions, and land-access permitting.

While array design parameters are well understood for traditional seismic deployments (e.g., Liner, 2016), this is not the case for DAS. Before DAS arrays are deployed in the field, it is prudent to first synthetically test their performance using established simulation methods to understand their theoretical sensitivity once deployed in the field. The goal of this paper is to investigate the sensitivity and ability of synthetic DAS arrays by testing various polygonal geometries. The performance of DAS arrays in relocating synthetic sources, as well as their sensitivity to noise, can guide eventual DAS deployment in the field and identify ideal array designs.

2 DAS amplitude response

Amplitudes of phases recorded by a linear segment of fiber is heavily controlled by the angle of incidence, θ, between the source and the fiber (Lindsey et al., 2020). For a P-wave, the amplitude of the wavefield recorded by DAS is scaled by $\cos^2\theta$ (Figure 1), meaning that a phase travelling parallel to the fiber segment has an amplitude scaling of 1, whereas a broadside (i.e., cable-perpendicular) arrival has a scaling of 0 (Mateeva et al., 2014; Lindsey and Martin, 2021). This has led to the use of winding, helical geometries for DAS measurements (Hornman, 2017; Yavuz et al., 2019; Mellors et al., 2021) to increase P-wave sensitivity (Kuvshinov, 2016) at the expense of S-wave sensitivity (Baird et al., 2020). However, these specialized fibers are rarely available and require an additional interrogator unit. Thus, we focus our attention on how the $\cos^2\theta$ amplitude scaling affects the more commonly used linear fiber arrays in recording P-waves.

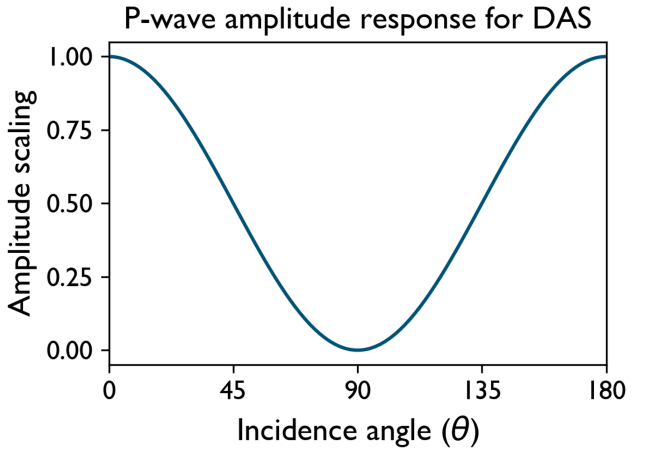

Figure 1 Theoretical DAS amplitude response for a P-wave arrival as a function of incidence angle.

While the $\cos^2\theta$ scaling is typically applied to the incidence angle between the DAS fiber and an upcoming wavefront, it is more generally a 3-D scaling. As a result, it can be assumed that a source-receiver geometry in the horizonal plane would also apply. That is, rather than incidence angle, the DAS data would be scaled as a function of the source-receiver backazimuth. Such behavior has been observed in a DAS array in a horizontal surface-seismic configuration with a shallow broadside source (Mateeva et al., 2014) as well as previous synthetic analysis of DAS array sensitivities (Kennett, 2022), confirming the applicability of the $\cos^2\theta$ scaling as a function of backazimuth to surficial DAS arrays.

For simplicity of the analysis, we focus on P-wave sensitivity of various regular polygons to simulate DAS array geometries that one may consider deploying in the field. These polygons are a balance between the omnidirectional sensitivity of circular arrays, the linearity required for 2-D frequency-wavenumber analysis, and deployment logistics. Our goals here are to (1) identify which DAS polygons exhibit the best performing steered response function given the $\cos^2\theta$ amplitude scaling and (2) test polygons performance in locating regional- and local-scale synthetic sources. To further investigate (2), the performance of a star-shaped array and a polygonal array in beamforming and back-projection are compared. This star-shaped array geometry is conceptualized as an antenna with linear segments to optimize wavefront propagation along the fiber axis while considering logistics of field deployments and minimizing doubling of the cabling.

3 Methods

Waveform simulations were run with PyFK (Zhu and Rivera, 2002; Xi et al., 2021) and the 1-D PREM velocity function (Dziewonski and Anderson, 1981). The resulting output provided vertical, radial, and transverse (ZRT) orientated synthetic displacement waveforms, which were further processed with the ObsPy library (Beyreuther et al., 2010). To convert from ZRT-oriented synthetic seismic data to synthetic DAS data, the radial component was rotated to be fiber parallel based on the backazimuth between the fiber segment and the synthetic source location (Figure 2). Then the fiber-parallel component waveform amplitude was scaled by $\cos^2\theta$ (Figure 2) to create a synthetic DAS recording. The angle between two channels on either side of a bend in the synthetic array is taken as the straight-line distance between the two. Bends in the array affect only a small number of channels (< 1 % of all channels), meaning the influence on beamforming and back-projection calculations are negligible. Finally, the data were trace normalized before analysis.

The conversion from synthetic seismic to synthetic DAS assumes that the PyFK output of displacement is proportional to strain-rate as recorded by DAS. These synthetic DAS timeseries were used for downstream beamforming and back-projection calculations. The relationship between a strain system (e.g., strain or strain-rate) and a ground motion system (e.g., displacement, velocity, acceleration) has been established by recent studies such as Bakku (2015) and Wang et al. (2018). Additionally, as shown in van den Ende and Ampuero (2021), conversion from strain-rate to velocity reduces artifacts observed when applying beamforming to DAS data. Therefore, we consider this downstream processing with ground-motion data a valid approximation.

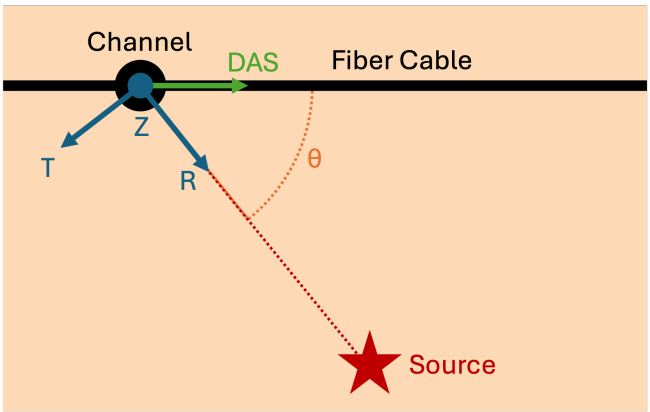

Figure 2 Map-view schematic of ZRT-to-DAS rotation.

While traditional delay-and-sum array response calculations are applicable to seismometers (e.g., Rost and Thomas, 2002), the sensitivity of the DAS array to the angle between the optical fiber and the incoming wavefront (Lindsey et al., 2020) requires the calculation of a steered response function (Näsholm et al., 2022; Kennett, 2022) which considers this directional sensitivity. This method also incorporates the modulation effect of slowness to account for the angular behavior of the arriving wave (Näsholm et al., 2022; Kennett, 2022).

To assess each array's performance, steered response functions were calculated using the numerical workflow of Näsholm et al. (2022). In this method, a vertically incident plane wave with a uniform arrival time across the array (i.e., a teleseismic phase traveling at infinite apparent velocity) was used to calculate a synthetic signal, with each trace scaled by the fiber-source incident angle θ using $\cos^2\theta$. Then, for each steering slowness, steering delays were applied to each trace to shift the signal. The time-shifted data are stacked, with the output power being the temporal average of the stack squared. The resulting 2-D steered response function can then be interpreted in a similar manner as a classical array response function (Näsholm et al., 2022; Kennett, 2022).

The features in the steered response function represent only the azimuthal component of the response, allowing for a comparison of array designs. The presence, amplitude, and orientation of side-lobes in steered response functions indicate backazimuths where aliasing may occur, as well as the apparent velocity of these aliased arrivals (Koper et al., 2009). This provides a high-level assessment of array performance as a function of apparent velocity and source-array geometries and is most applicable to far-field sources.

For regional sources, beamforming was performed using the same algorithm used to calculate steered response functions (Näsholm et al., 2022). Synthetic sources were used to calculate synthetic waveforms for each receiver with PyFK such that, rather than assess the characterization of a vertically incident plane wave, this test simulates a real-world seismic event. Beamforming was performed using a 5-second window of data which captured the first P-wave arrival across the array. The location of the main lobe in cartesian slowness space provides the backazimuth between the array and the source (Koper et al., 2009; Näsholm et al., 2022; Kennett, 2022).

For local sources, a 2-D back-projection was performed using the synthetic waveforms (Fee et al., 2021). Envelopes were calculated and first arrivals were isolated in the synthetic waveforms using a τ-p solver (Crotwell et al., 1999). Next, a grid of possible source locations was used to estimate travel times using a straight-line distance and a constant velocity of 5.8 km/s for each source-receiver pair, consistent with the shallow-most P-wave velocity from PREM (Dziewonski and Anderson, 1981). The envelopes are shifted by their respective estimated travel time and stacked for each possible source location. The node which produces the maximum stack function is taken as the recovered source location.

To test the performance of the DAS array in a real-world setting, synthetic Earth noise was applied at varying amplitudes to the synthetic data using the power spectrum of the Peterson (1993) New Low Noise Model (NLNM). The NLNM is a composite model of spectra obtained from stations deployed in a variety of settings that represent quiet microseismic periods. This is a hypothetical background noise spectrum that represents average noise observed globally. While this spectrum may not be observed at any specific location, for our

purposes it simulates more realistic Earth noise conditions than purely stochastic noise and is less subjective than manually constructed noise (e.g., Tibi et al., 2022). Noise amplitude was scaled to achieve prescribed signal-to-noise ratios (SNR) between infinity (i.e., no noise) and 1 to simulate a variety of noise levels (Figure 3). To achieve each SNR, the synthetic noise was scaled relative to the maximum of the synthetic P-wave arrival, then summed with the synthetic DAS trace. At a SNR of 1, the synthetic noise is the same amplitude as the synthetic P-wave arrival. As a result, the noise destructively adds to the signal to such a degree that the arrival is obscured.

The noise was applied with a constant phase and small random perturbations (Porritt and Stanciu, 2023), with each channel in the simulation having the same SNR. The noisy synthetic data was then used to calculate beamforming and back-projection results, with the change in error recorded as a function of the SNR. The global peak in the beamforming slowness field was used to calculate the recovered backazimuth, which was compared to the true backazimuth between the array and the source to calculate the backazimuth error. The Euclidian distance between the back-projection recovered epicenter and the true epicenter was used to calculate the location error. These results act as a proxy for source magnitude and/or variations in local noise conditions, providing insight into the minimum detectability threshold for DAS arrays.

4 Results

We calculated steered response functions for various regular polygons with a total synthetic DAS fiber length of 1 km and a gauge length of 3 m, producing an array with an aperture of ~250 m (Figure 4 insets). We limited the synthetic tests to DAS array shapes composed of linear segments, which are straightforward to convert into the frequency-wavenumber space for translation between strain-rate and ground velocity (e.g., Bakku, 2015; Wang et al., 2018). The source was a 0.1-sec Ricker wavelet recorded at 100 samples per second for 2 seconds and given a slowness of 0 s/km. These calculations simulate a vertically incident plane wave arriving at all channels simultaneously (i.e., a teleseismic phase with infinite apparent velocity).

Four examples of these calculations are shown in Figure 4. All four examples exhibit side lobes within the expected range of crustal velocities (4–8 km/s; red contours in Figure 4), indicating these geometries may record aliased arrivals exhibiting these apparent velocities. However, the pentagon and heptagon produce noticeably smaller amplitude side lobes (Figure 4A, C). To quantify this side lobe suppression, we calculated the steered response amplitude ratio between the main lobe and the maximum side lobe for each polygon. Generally, the lobe ratios are higher (i.e., better) for odd-sided polygons than for even-sided polygons (Figure 4). To examine this behavior further, we calculated the lobe ratios for polygons with up to 25 sides (Figure 4E). For polygons with N-sides $<$ ~10, higher ratios are observed for odd-sided polygons compared to even-sided polygons. For N-sides $>$ ~10, this difference is diminished, presumably because the side lengths of the polygons are decreasing and the overall geometry of the DAS array is beginning to approach a circle as N-sides increases. Of the polygons examined in Figure 4A–D, the heptagon exhibits the most ideal steered response and has the most suppressed sidelobes (Koper et al., 2009). Thus, we take the heptagon to be the 'ideal' geometry of the polygons tested.

To simulate example experiment designs, two general geometries were tested: a star shape (Figure 5A) and a heptagon (Figure 5B). The array aperture for these geometries is increased to ~500 m to simulate a small-scale field deployment. These array designs simulate an experiment where an interrogator is placed at some stand-off distance and connected to the test array via a bridge cable. As expected from the results shown in Figure 4, the heptagon produces smaller side and main lobes in the steered response function (Figure 5B). The lobe ratio is higher for the heptagon (1.68) than for the star (1.31). An additional benefit of the heptagon over the star geometry in this case is that the heptagon requires about half the length of fiber as the star geometry, reducing costs as well as field logistics.

To examine the performance of these arrays' ability to record local to near-regional sources, we perform forward modelling and subsequent beamforming of synthetic sources. A 1-second-long source time function was applied to a 60-second Green's Function using PREM P-wave velocities sampled at 200 samples per second for a source ~116 km away from the center of the array (Figure 6A). This source-array distance is arbitrarily chosen to represent an array recording an event at near-regional distance. A 5-second window taken at ~20 seconds after the origin time was used for the beamform calculation. These results are summarized in Figure 6. The main lobe in the star response function (Figure 6B) is relatively wide compared to the main lobe of the heptagon (Figure 6C). However, while the star geometry sidelobes fall outside the -8 dB contour in Figure 6B, both the heptagon main lobe and sidelobes are within the -8 dB power level. This highlights that the narrower heptagon main lobe comes at the expense of higher amplitude sidelobes.

Since beamforming characterizes a passing plane wave (i.e., a teleseismic arrival), steered responses are not as applicable to investigating the ability of an array to record local sources where the propagation is not a single plane wave. Because of this, back-projection was performed on forward modelled synthetic sources for the star-shaped and heptagon geometries at the end of a linear segment. These array designs simulate an experiment where an interrogator is placed at some stand-off distance and connected to the test array via a bridge cable. A source with a depth of 0 km was placed near the center of the terminal shape of both arrays to test how well the differing geometries could recover the epicenter and origin time. The back-projection grid search was performed on a 50-by-50 grid (i.e., 60 m node spacing). Recovered locations were limited to grid nodes, whereas input source locations were randomly dispersed. The recovery results are shown in Figure 7.

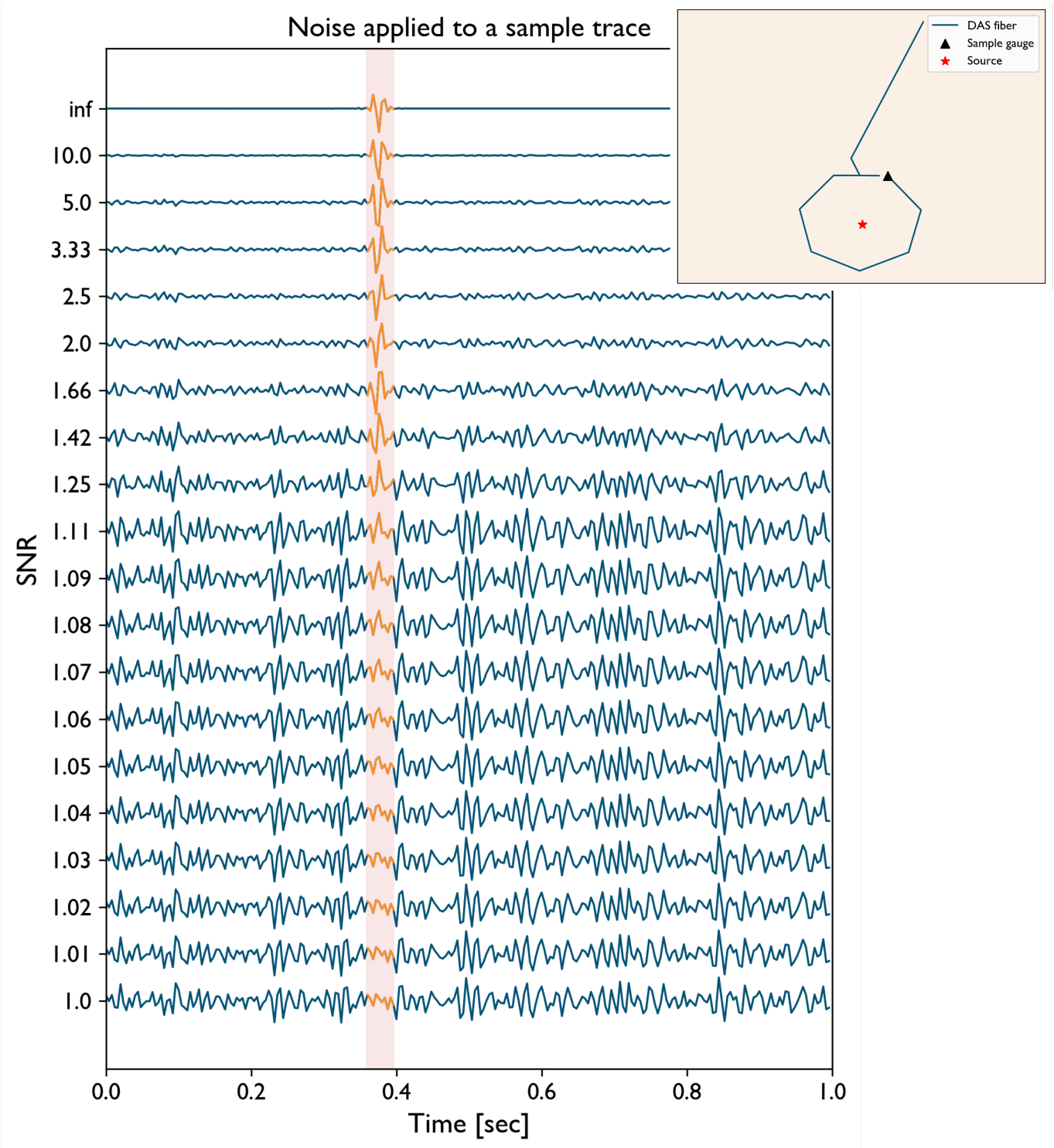

Figure 3 Sample synthetic DAS trace with simulated Earth noise scaled to SNR values from infinity (i.e., no noise) to 1. Synthetic arrival highlighted. All waveforms have been trace-normalized after noise application. Inset: DAS fiber and sample channel-receiver geometry.

While both geometries were able to recover this source location to within one grid node for some synthetic source locations, subtle differences in the back-projection amplitude field reveal how the source-receiver geometry and DAS $\cos^2\theta$ waveform amplitude scaling may influence location results and associated errors. When the heptagon sides are ~90° to the source (e.g., Figure 7D), little amplitude information is recorded by this portion of the DAS array, causing the linear segments to contribute more to the back-projection solution. This has the added result of smearing back-projection amplitudes perpendicularly to the linear segments. In contrast, because the linear segments of the star geometry are all approximately parallel to the source-receiver backazimuth, they record higher amplitudes (i.e., Figure 1) and contribute more to the recovered location solution.

To test the sensitivity of a linear DAS array with a terminal heptagon (i.e., Figure 3 inset) in a real-world noise environment, relocation errors were cal-

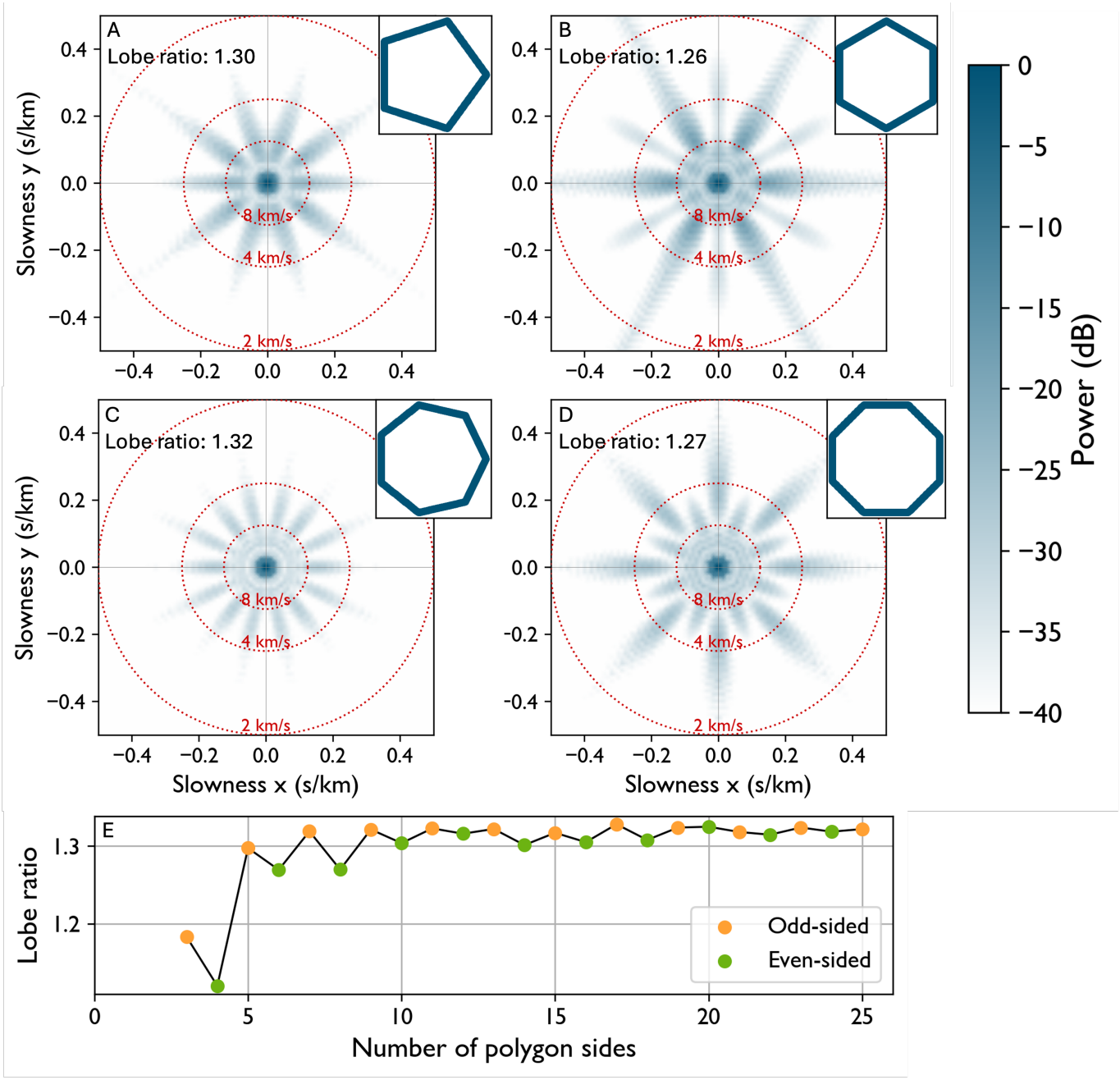

Figure 4 Steered responses as a function of regular polygonal geometries. A 3 m gauge length synthetic DAS array with a fiber arranged in a (A) pentagon, (B) hexagon, (C) heptagon, (D) and octagon. Red contours show relevant crustal apparent velocities. E provides main lobe-to-sidelobe amplitude ratios for polygons with 3 to 25 sides.

culated for a variety of SNR values (Figure 3) for back-projection (Figure 8A) and beamforming (Figure 8B) results. The beamforming and back-projection calculations were performed using source-array geometries discussed previously (Figure 8 insets). For comparison, the SNR-sensitivity of synthetic seismometer arrays with the same geometry as the synthetic DAS were also tested (Figure 8). These included seismometer arrays with instrument spacings of 100, 250, and 500 m. The vertical component calculated using PyFK (Zhu and Rivera, 2002; Xi et al., 2021) was used in these calculations, without the application of the in-line rotation or $\cos^2\theta$ amplitude scaling used for the synthetic DAS records.

5 Discussion

Example DAS arrays with regular polygonal geometries demonstrate that odd-sided polygons—that is, polygons with no parallel sides—produce improved steered response functions by suppressing alias side lobes (Figure 4). We suspect that this is a result of the $\cos^2\theta$ amplitude scaling behavior of DAS. Because even-sided polygons have parallel sides, these segments of the DAS fiber constructively add their respective response functions, amplifying the alias lobes generated by their linearity. In contrast, odd-sided polygons do not have parallel sides, so this constructive interference does not occur in the steered response calculation, resulting in suppression of side lobes. This suggests that, in the case

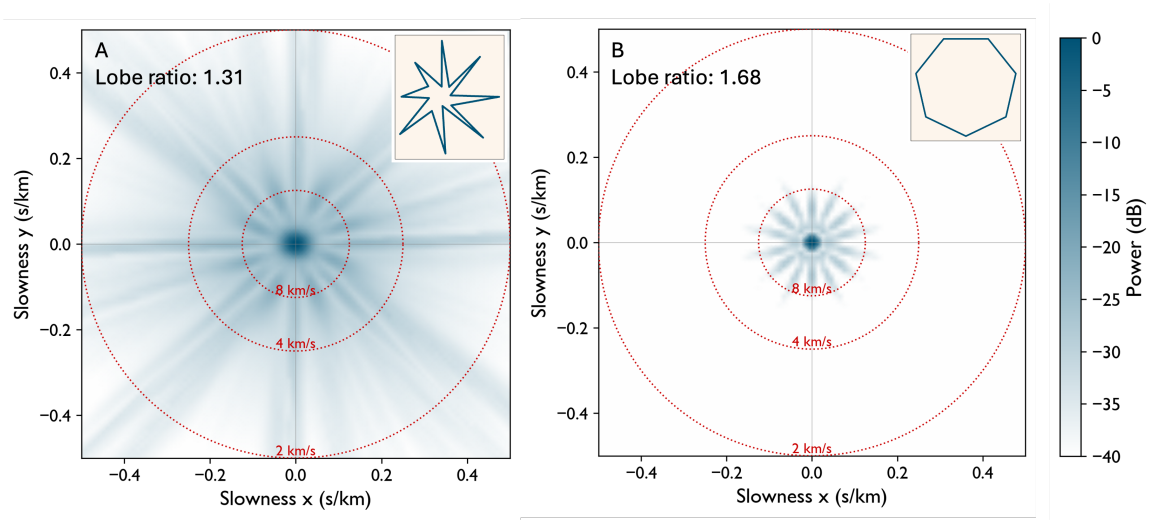

Figure 5 Steered response functions for a star DAS array geometry (A) and a heptagon geometry (B).

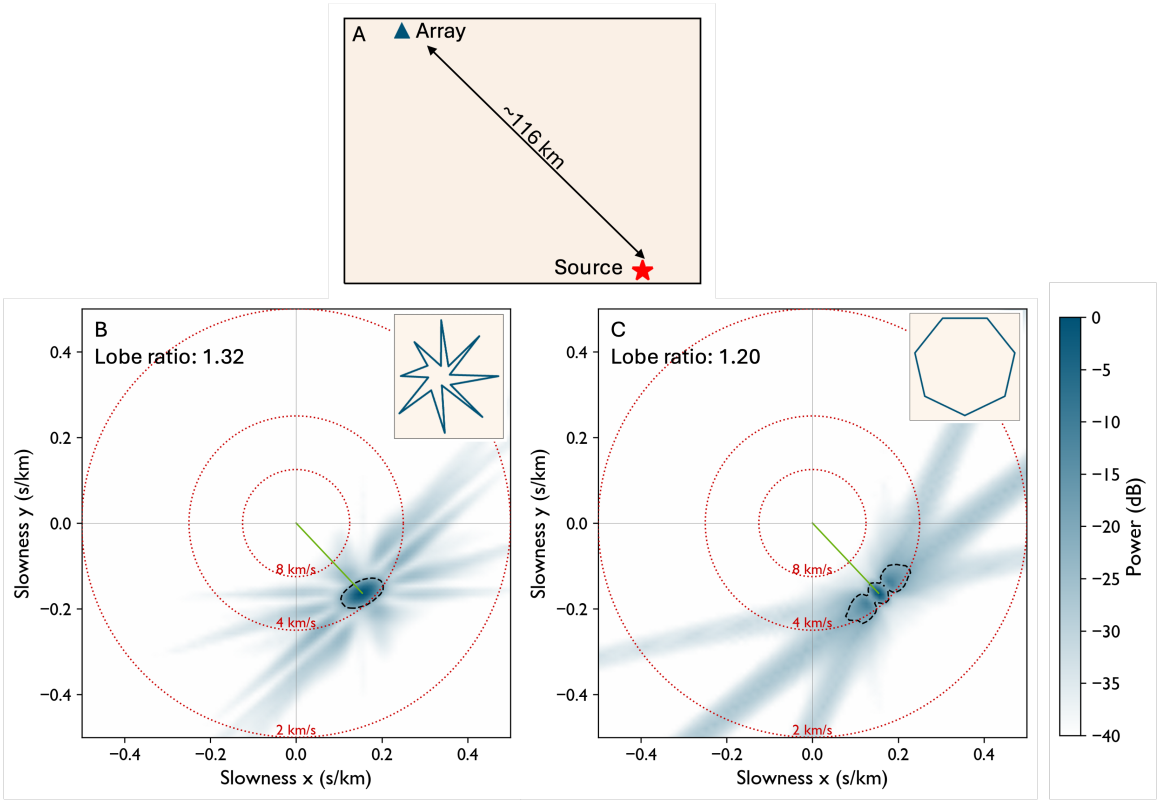

Figure 6 Beamforming results using steered response functions for a regional source. (A) Relative location of the source and array at ~116 km distance. (B) The linear-star geometry and corresponding steered response with larger main lobe but suppressed side lobes. (C) The linear-heptagon geometry and steered response with smaller main lobes but higher amplitude side lobes. Black contours highlight -8 dB power level. Red contours show relevant apparent velocities.

of regional- to teleseismic-scale experiments, an odd-sided polygon is a preferrable geometry for a DAS array (e.g., Figure 4A, C).

A heptagon significantly reduces steered response function sidelobe size and amplitudes compared to a star geometry (Figure 5). Yet, when performing beamforming of a regional source, the area of the heptagon main lobe is reduced at the expense of higher sidelobe amplitudes (Figure 6), suggesting that heptagon arrays may be better suited for teleseismic studies over regional studies.

For a smaller DAS deployment designed to investigate local sources, there may also be added benefits by incorporating an odd-sided polygon with a linear array due to the increased sensitivity of source-receiver backazimuths (i.e., Figure 7). Back-projection errors of a local source with an epicenter near the center of the terminal polygon (Figure 7B, D) appears to be controlled by the polygon's geometry. In the case of the star shape, multiple segments of the star are aligned well with the source, given the DAS $\cos^2\theta$ amplitude scaling, and the segments contribute more to the back-projection calcu-

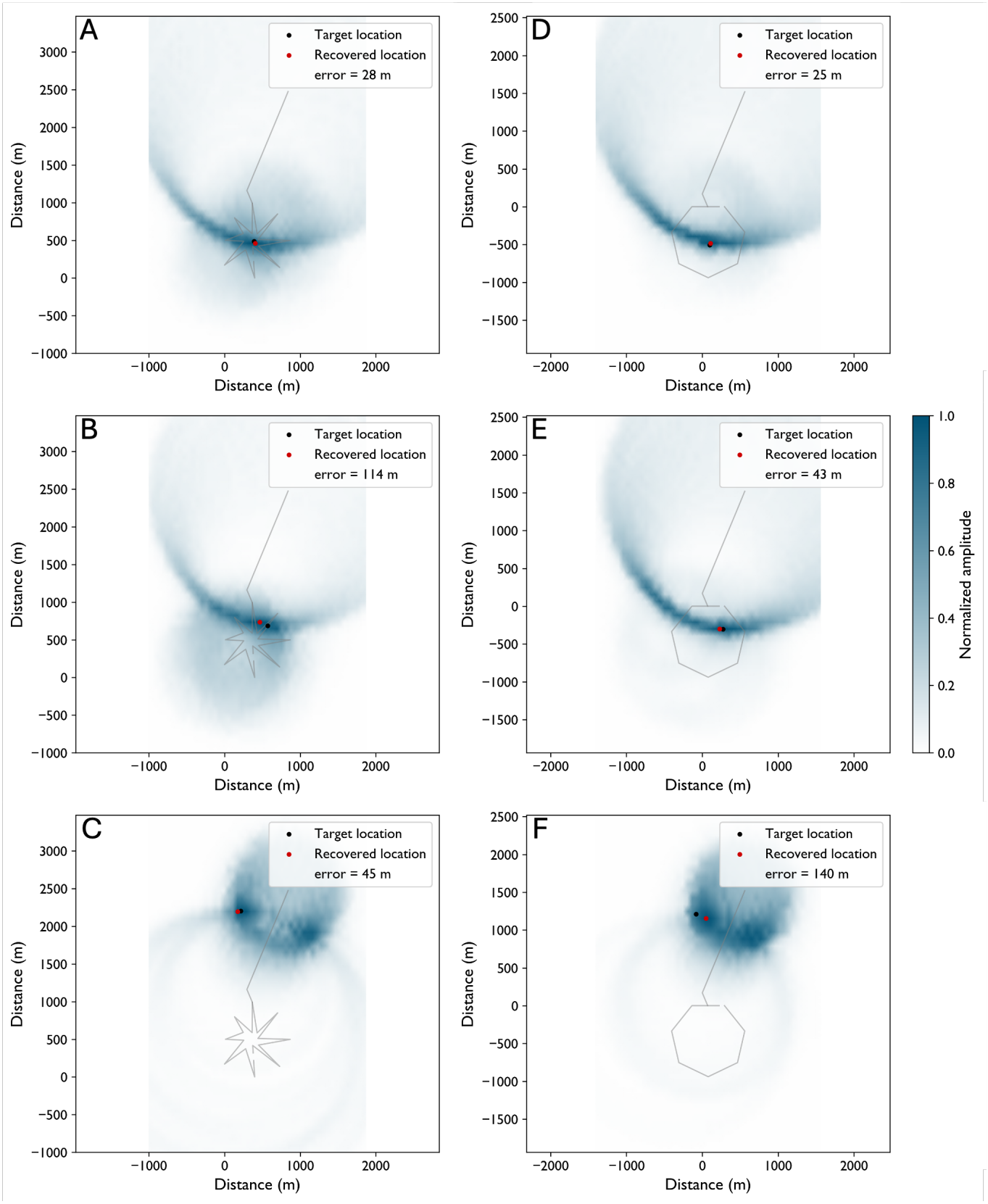

Figure 7 Relocated epicenters for synthetic sources as recovered by a linear-star geometry (A–C) and by a linear-heptagon geometry (D–F). Black circle is synthetic source epicenter and red circle is the location recovered through back-projection.

lation. This is in addition to the linear portion of the array, which is also well aligned with the source location. The error associated with this geometry in the back-projection calculation is thus more uniform around the recovered location (Figure 7). In contrast, the heptagon geometry results in more broadside source-receiver orientations, meaning the polygon contributes less to the back-projection calculation. This leaves the linear segment of the array to contribute more to the location calculation. The consequence of this is that the error is

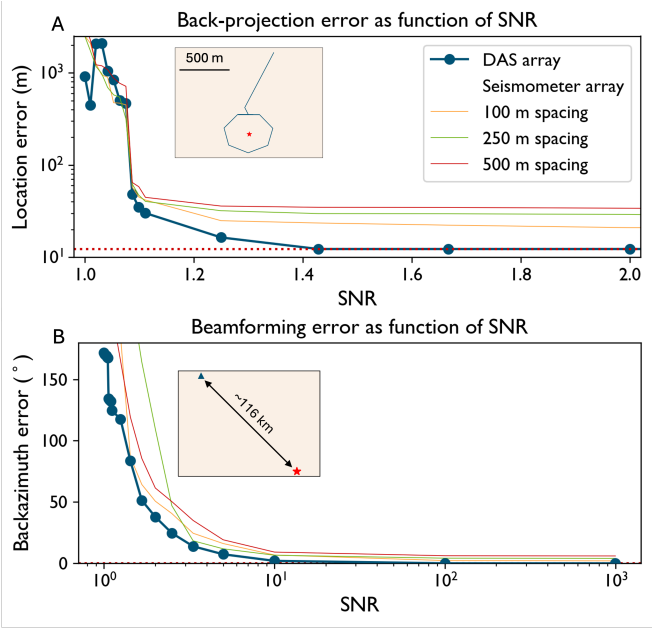

Figure 8 Error as a function of SNR from (A) back-projection and (B) beamforming of a synthetic source. Dashed red line shows baseline error calculated before the addition of noise. The performance of synthetic seismometer arrays deployed in the same geometry with 100 m (orange), 250 m (green), and 500 m (red) instrument spacing is shown for comparison. Inset map shows source-array geometries.

much more elongated and elliptical, oriented perpendicular to the linear segment (Figure 7). While both geometries perform relatively well in recovering the epicenter of the synthetic source, the difference in the location errors should be taken into consideration when designing an array to capture a local source.

When the source is slightly off-center inside the polygon, the star array produces errors equivalent to ~2 grid cells (Figure 7B) while the heptagon still performs well with errors $<$ 1 grid cell (Figure 7E). However, when the source is placed outside the array, the heptagon error is $>$ 2 grid cells (Figure 7F) whereas the star array is $<$ 1 grid cell (Figure 7C). This exemplifies the need to carefully consider how a proposed DAS array is designed around either ground zero, in the case of a chemical explosion, or the general region where earthquake sources are expected to occur.

The ability of these synthetic tests to recover the source backazimuth appears to be more sensitive to the SNR than back-projection location recovery (Figure 8). Even at high SNR values (i.e., an SNR factor of 10) the backazimuth error is no better than ~20°. This contrasts with back-projection errors, which remain constant for SNR values $>$ 1.5. Only below an SNR of ~1.4 does the recovered location begin to shift due to noise-induced error, reaching an error of $>$ 50 m at an SNR of ~1.1. Below this SNR, the errors become greater than one kilometer. This suggests that regional source relocation is more sensitive to noise than local source relocation, which is consistent with the established behavior of relocation methods using traditional seismic records.

For comparison, as synthetic seismometer instrument spacing increases, the baseline, infinite-SNR error also increases (Figure 8). At these high SNR values, DAS generally outperforms the seismic arrays. However, as the SNR decreases, the noise levels appear to overcome the relative effects of instrument spacing, with both DAS and seismometer arrays performing poorly below SNRs of ~1.1 for back-projection (Figure 8A) and SNR of ~5 for beamforming (Figure 8B).

6 Conclusions

DAS provides a high-density endmember to the large-N spectrum of seismic deployments but has mainly relied on pre-installed telecommunication fibers in previous experiments, limiting our understanding of ideal array design principles. We have presented synthetic calculations of steered responses, beamforming, and back-projection which have helped reveal subtle DAS array behavior. Odd-sided polygonal DAS geometries produced improved sensitivity by suppressing steered response side lobes, likely due to the $\cos^2\theta$ waveform amplitude response of DAS. In beamforming of regional sources, a heptagon produces a tighter main lobe at the expense of higher sidelobe amplitudes compared to a star geometry while being relatively sensitive to SNR. Near-field, local source location recovery appears to be more complicated, with heptagons performing well when sources are within the polygon perimeter but is generally less sensitive to SNR. While not an exhaustive exploration of DAS array performance, these synthetic tests of DAS array geometries and array-source orientations do highlight the importance of theoretically exploring the research problem prior to installing a DAS array. This result also demonstrates the additional work the geophysical community must complete to bring our collective understanding of DAS array design principles to the level of traditional seismic arrays.

Acknowledgements

We wish to thank Rob Abbott, Christian Stanciu, and Rigo Tibi for their insightful discussions. We also wish to thank the editors and one anonymous reviewer for their comments and suggestions which significantly improved this manuscript.

This Source Physics Experiment (SPE) research was funded by the National Nuclear Security Administration, Defense Nuclear Nonproliferation Research and Development (NNSA DNN R&D). The authors acknowledge important interdisciplinary collaboration with scientists and engineers from LANL, LLNL, NNSS, and SNL.

This Ground-based Nuclear Detonation Detection (GNDD) research was funded by the National Nuclear Security Administration, Defense Nuclear Nonproliferation Research and Development (NNSA DNN R&D). The authors acknowledge important interdisciplinary collaboration with scientists and engineers from Sandia National Laboratories.

Sandia National Laboratories is a multi-mission laboratory managed and operated by National Technology and Engineering Solutions of Sandia, LLC, a wholly

owned subsidiary of Honeywell International, Inc., for the U.S. Department of Energy's National Security Administration under contract DE-NA-0003525.

Data and code availability

The codes used for beamforming, back-projection, and noise simulation can be found at Sandia National Laboratories GitHub (https://github.com/sandialabs).

Competing interests

The authors declare that they have no competing interests.

References

Baird, A. F., Stork, A. L., Horne, S. A., Naldrett, G., Kendall, J.-M., Wookey, J., Verdon, J. P., and Clarke, A. Characteristics of microseismic data recorded by distributed acoustic sensing systems in anisotropic media. *GEOPHYSICS*, 85(4):KS139–KS147, June 2020. doi: 10.1190/geo2019-0776.1.

Baker, M. G. and Abbott, R. E. Rapid refreezing of a marginal ice zone across a seafloor distributed acoustic sensor. *Geophysical Research Letters*, 49(24), Dec. 2022. doi: 10.1029/2022gl099880.

Bakku, S. Fracture characterization from seismic measurements in a borehole, 2015.

Beyreuther, M., Barsch, R., Krischer, L., Megies, T., Behr, Y., and Wassermann, J. ObsPy: A Python toolbox for seismology. *Seismological Research Letters*, 81(3):530–533, May 2010. doi: 10.1785/gssrl.81.3.530.

Crotwell, H. P., Owens, T. J., and Ritsema, J. The TauP toolkit: Flexible seismic travel-time and ray-path utilities. *Seismological Research Letters*, 70(2):154–160, Mar. 1999. doi: 10.1785/gssrl.70.2.154.

Dando, B., Iranpour, K., Wuestefeld, A., Näsholm, S. P., Baird, A., and Oye, V. Designing the next generation of seismic arrays using fibre optic DAS. Mar. 2022. doi: 10.5194/egusphere-egu22-6408.

Dou, S., Lindsey, N., Wagner, A. M., Daley, T. M., Freifeld, B., Robertson, M., Peterson, J., Ulrich, C., Martin, E. R., and Ajo-Franklin, J. B. Distributed acoustic sensing for seismic monitoring of the near surface: A traffic-noise interferometry case study. *Scientific Reports*, 7(1), Sept. 2017. doi: 10.1038/s41598-017-11986-4.

Dziewonski, A. M. and Anderson, D. L. Preliminary reference Earth model. *Physics of the Earth and Planetary Interiors*, 25(4): 297–356, June 1981. doi: 10.1016/0031-9201(81)90046-7.

Fang, G., Li, Y. E., Zhao, Y., and Martin, E. R. Urban near-surface seismic monitoring using distributed acoustic sensing. *Geophysical Research Letters*, 47(6), Mar. 2020. doi: 10.1029/2019gl086115.

Fee, D., Toney, L., Kim, K., Sanderson, R. W., Iezzi, A. M., Matoza, R. S., De Angelis, S., Jolly, A. D., Lyons, J. J., and Haney, M. M. Local explosion detection and infrasound Localization by Reverse Time Migration Using 3-D Finite-Difference Wave Propagation. *Frontiers in Earth Science*, 9, Feb. 2021. doi: 10.3389/feart.2021.620813.

Hornman, J. Field trial of seismic recording using distributed acoustic sensing with broadside sensitive fibre-optic cables. *Geophysical Prospecting*, 65(1):35–46, Jan. 2017. doi: 10.1111/1365-2478.12358.

IRIS Data Management Center. EarthScope data statistics, 2023. https://ds.iris.edu/data/distribution/.

Kennett, B. L. N. The seismic wavefield as seen by distributed acoustic sensing arrays: Local, regional and teleseismic sources. *Proceedings of the Royal Society A: Mathematical, Physical and Engineering Sciences*, 478(2258), Feb. 2022. doi: 10.1098/rspa.2021.0812.

Koper, K. D., de Foy, B., and Benz, H. Composition and variation of noise recorded at the Yellowknife Seismic Array, 1991–2007. *Journal of Geophysical Research: Solid Earth*, 114(B10), Oct. 2009. doi: 10.1029/2009jb006307.

Kuvshinov, B. Interaction of helically wound fibre-optic cables with plane seismic waves. *Geophysical Prospecting*, 64(3): 671–688, May 2016. doi: 10.1111/1365-2478.12303.

Lindsey, N. J. and Martin, E. R. Fiber-optic seismology. *Annual Review of Earth and Planetary Sciences*, 49(1):309–336, May 2021. doi: 10.1146/annurev-earth-072420-065213.

Lindsey, N. J., Dawe, T. C., and Ajo-Franklin, J. B. Illuminating seafloor faults and ocean dynamics with dark fiber distributed acoustic sensing. *Science*, 366(6469):1103–1107, Nov. 2019. doi: 10.1126/science.aay5881.

Lindsey, N. J., Rademacher, H., and Ajo-Franklin, J. B. On the broadband instrument response of fiber-optic DAS arrays. *Journal of Geophysical Research: Solid Earth*, 125(2), Feb. 2020. doi: 10.1029/2019jb018145.

Liner, C. L. *Elements of 3D seismology*. Society of Exploration Geophysicists, Jan. 2016. doi: 10.1190/1.9781560803386.

Mateeva, A., Lopez, J., Potters, H., Mestayer, J., Cox, B., Kiyashchenko, D., Wills, P., Grandi, S., Hornman, K., Kuvshinov, B., Berlang, W., Yang, Z., and Detomo, R. Distributed acoustic sensing for reservoir monitoring with vertical seismic profiling. *Geophysical Prospecting*, 62(4):679–692, May 2014. doi: 10.1111/1365-2478.12116.

Mellors, R. J., Abbott, R., Steedman, D., Podrasky, D., and Pitarka, A. Modeling subsurface explosions recorded on a distributed fiber optic sensor. *Journal of Geophysical Research: Solid Earth*, 126(12), Nov. 2021. doi: 10.1029/2021jb022690.

Näsholm, S. P., Iranpour, K., Wuestefeld, A., Dando, B. D. E., Baird, A. F., and Oye, V. Array signal processing on distributed acoustic sensing data: Directivity effects in slowness space. *Journal of Geophysical Research: Solid Earth*, 127(2), Feb. 2022. doi: 10.1029/2021jb023587.

Peterson, J. R. Observations and modeling of seismic background noise. Open-File Report 93-322, US Geological Survey, 1993.

Porritt, R. and Stanciu, A. An analysis of published DAS studies for application to SPE Phase III. Technical report, Office of Scientific and Technical Information (OSTI), Aug. 2023. doi: 10.2172/2430480.

Rost, S. and Thomas, C. Array seismology: Methods and applications. *Reviews of Geophysics*, 40(3), Sept. 2002. doi: 10.1029/2000rg000100.

Snelson, C., Bradley, C., Walter, W., Antoun, T., Abbott, R., Jones, K., Chipman, V., and Montoya, L. The Source Physics Experiment (SPE) Science Plan. Technical report, Office of Scientific and Technical Information (OSTI), Sept. 2022. doi: 10.2172/1887003.

Snelson, C. M., Abbott, R. E., Broome, S. T., Mellors, R. J., Patton, H. J., Sussman, A. J., Townsend, M. J., and Walter, W. R. Chemical explosion experiments to improve nuclear test monitoring. *Eos, Transactions American Geophysical Union*, 94(27):237–239, July 2013. doi: 10.1002/2013eo270002.

Tibi, R., Young, C. J., and Porritt, R. W. Comparative study of the performance of seismic waveform denoising methods using local and near-regional data. *Bulletin of the Seismological Society of America*, 113(2):548–561, Dec. 2022. doi: 10.1785/0120220105.

van den Ende, M. P. A. and Ampuero, J.-P. Evaluating seismic beamforming capabilities of distributed acoustic sensing arrays. *Solid Earth*, 12(4):915–934, Apr. 2021. doi: 10.5194/se-12-915-2021.

Wang, H. F., Zeng, X., Miller, D. E., Fratta, D., Feigl, K. L., Thurber, C. H., and Mellors, R. J. Ground motion response to an ML 4.3 earthquake using co-located distributed acoustic sensing and seismometer arrays. *Geophysical Journal International*, 213(3): 2020–2036, Mar. 2018. doi: 10.1093/gji/ggy102.

Wang, X., Williams, E. F., Karrenbach, M., Herráez, M. G., Martins, H. F., and Zhan, Z. Rose parade seismology: Signatures of floats and bands on optical fiber. *Seismological Research Letters*, 91 (4):2395–2398, May 2020. doi: 10.1785/0220200091.

Xi, Z., Li, J., Chen, M., and Wei, S. PyFK: A fast MPI and CUDA accelerated Python package for calculating synthetic seismograms based on the frequency-wavenumber method. In *AGU Fall Meeting Abstracts*, 2021.

Yavuz, S., Freifeld, B., Pevzner, R., Dzunic, A., Ziramov, S., Bóna, A., Correa, J., Tertyshnikov, K., Urosevic, M., Robertson, M., and Daley, T. The initial appraisal of buried DAS system in CO2CRC Otway Project: The comparison of buried standard fibre-optic and helically wound cables using 2D imaging. *Exploration Geophysics*, 50(1):12–21, Jan. 2019. doi: 10.1080/08123985.2018.1561147.

Zhu, L. and Rivera, L. A. A note on the dynamic and static displacements from a point source in multilayered media. *Geophysical Journal International*, 148(3):619–627, Mar. 2002. doi: 10.1046/j.1365-246x.2002.01610.x.